Research Square

Preprints are preliminary reports that have not undergone peer review.
They should not be considered conclusive, used to inform clinical practice,
or referenced by the media as validated information.

Control of Dynamic sp3-C Stereochemistry

Aisha Bismillah
Durham University
Toby Johnson
Durham University
Burhan Hussein
Durham University
Andrew Turley
Durham University
Ho Chi Wong
Durham University
Juan Aguilar
Durham University
Dmitry Yufit
Durham
Paul McGonigal (paul.mcgonigal@durham.ac.uk)
Durham University https://orcid.org/0000-0002-8538-7579

Article

Keywords: stereochemistry, Stereogenic sp3-hybridized carbon

Posted Date: March 26th, 2021

DOI: https://doi.org/10.21203/rs.3.rs-318491/v1

License: This work is licensed under a Creative Commons Attribution 4.0 International License.
Read Full License

Control of Dynamic sp^3-C Stereochemistry

Aisha N. Bismillah,[‡] Toby G. Johnson,[‡] Burhan A. Hussein, Andrew T. Turley, Ho Chi Wong, Juan A. Aguilar, Dmitry S. Yufit, Paul R. McGonigal*

Department of Chemistry, Durham University, Lower Mountjoy, Stockton Road, Durham, DH1 3LE, United Kingdom

[‡] These authors contributed equally to this work.

* To whom correspondence should be addressed. E-mail: paul.mcgonigal@durham.ac.uk

Abstract: **Stereogenic sp^3-hybridized carbon centres are fundamental building blocks of chiral molecules. Unlike dynamic stereogenic motifs, such as sp^3-nitrogen centres or atropisomeric biaryls, sp^3-carbon centres are usually fixed, requiring intermolecular reactions to undergo configurational change. Here, we report the internal enantiomerization of fluxional carbon cages and the consequences of their adaptive configurations for the transmission of stereochemical information. The sp^3-carbon stereochemistry of the rigid tricyclic cages is inverted through strain-assisted Cope rearrangements, emulating the low-barrier configurational dynamics typical for sp^3-nitrogen inversion or conformational isomerism. This dynamic enantiomerization can be stopped, restarted, or slowed by external reagents, while the configuration of the cage is controlled by neighbouring, fixed stereogenic centres. As part of a phosphoramidite–olefin ligand, the fluxional cage acts as a conduit to transmit stereochemical information from the ligand while also transferring its dynamic properties to chiral-at-metal coordination environments, influencing catalysis and ligand exchange energetics.**

The hugely varied three-dimensional structures—and therefore the hugely varied properties—of many organic molecules emerge from combining just a few types of atomic building blocks. For example, 19 of the 22 proteinogenic amino acids are formed solely from sp^2- or sp^3-hybridized carbon, nitrogen, and oxygen atoms, capped by hydrogen substituents. Of this small array of elemental building blocks, it is tetrahedral sp^3-carbon[1–4] and sp^3-nitrogen[5–10] atoms that have the potential to form stereogenic centres, creating chiral structures.

Chirality also arises in organic molecules by virtue of motifs other than stereogenic atoms. But while some planar chiral motifs,[11–13] helices,[14–16] and atropisomeric bonds,[3] as well as stereogenic sp^3-nitrogen centres,[7–10] change configuration rapidly and reversibly through low-barrier processes, sp^3-carbon centres cannot generally undergo spontaneous inversion. For example, the energy barrier to pyramidal inversion of methane is greater than its C−H bond dissociation energy.[17,18] Unlike other stereogenic motifs,[11–16] therefore, sp^3-carbon centres cannot generally adapt their configuration to surrounding chiral moieties and cannot be controllably switched by the application of external stimuli.

Instead, intermolecular reactions are usually necessary[19,20] to invert individual stereogenic carbon centres, proceeding through stepwise mechanisms involving high-energy bond-breaking and bond-making steps[21] with pentavalent transition states[19] or trigonal intermediates,[20] such as carbocations, carbanions or radicals. Of course, it is this stability of sp^3-carbon's tetrahedral geometry that makes it essential to the chiral skeletal diversity of organic compounds. It allows for predictable synthesis of configurationally stable molecules. Yet, the stability also limits the extent to which the complex three-dimensional connectivity of aliphatic structures can exhibit dynamic, adaptive stereochemistry.[22]

There have been impressive, but rare, examples of small covalent systems[23–26] capable of sp^3-carbon enantiomerization by low-barrier intramolecular processes. However, they do so without external control of their rate or direction to a single stereoisomer. Only multicomponent interlocked

molecules, in which a ring shuttles along a prochiral axle,[27,28] have been amenable to external control. There have been no compact and controllable dynamic sp^3-carbon building blocks. Therefore, it has not been possible to investigate the transmission of stereochemical information through such systems.[7,9,10]

Here, we report a series of chiral fluxional carbon cages[29] that exhibit responsive sp^3-carbon-centered stereochemistry, adapting to and transmitting surrounding stereochemical information. By applying DFT calculations, solution- and solid-state NMR spectroscopy, in combination with X-ray crystallography, we establish the extent to which their dynamic Cope rearrangements are controlled by neighbouring, fixed stereogenic centres. We have found that a significant energetic bias of more than 10 $kJ \cdot mol^{-1}$ can be exercised over the stereochemical equilibria by a single fixed stereocentre. The rearrangements proceed rapidly at rates more commonly associated with conformational changes of aliphatic systems (e.g., a cyclohexane ring flip of ~43 $kJ \cdot mol^{-1}$) rather than a configurational change. We show that these rapid constitutional dynamics can be halted by covalent modification of the cage through a cycloaddition reaction, then subsequently restarted after a cycloreversion. The rearrangement rate is also attenuated upon coordination of the fluxional cage to Pd(II) or Ru(II) as part of a phosphoramidite–olefin ligand. By its inclusion in the simple ligand design, the fluxional cage transmits stereochemical information from a distal, fixed stereogenic centre to the metal ion. This property is exploited in enantioselective catalysis of a conjugate addition reaction and in creating chiral-at-metal stereogenic centres that adopt the configurational dynamics of the cage.

Results

The Cope rearrangement of barbaralane, **BB**, is an example (Fig. 1a) of a narcissistic[24,30] automerization—it gives rise to a degenerate structure through a transition state, TS-**BB**, bearing an internal mirror plane (σ_v') that is not present in the ground-state structure. We noted that by desymmetrizing **BB** (Fig. 1b) using either a 9-BB, 3-BB, or 2,4-BB substitution pattern, the mirror

plane present in the ground state (σ_v'') is lost while the mirror plane formed in the transition state (σ_v') is retained. As a result, the Cope rearrangement inverts simultaneously some, or all, of the four or five stereogenic centres present in the structure. Given that the rearrangement of **BB** is known to proceed with a remarkably low Gibbs free energy of activation, $\Delta G^{\ddagger}$, of 32.3 kJ·mol^{-1} (Table S3),[31–35] chiral 9-BB, 3-BB, or 2,4-BB derivatives should undergo rapid enantiomerization.

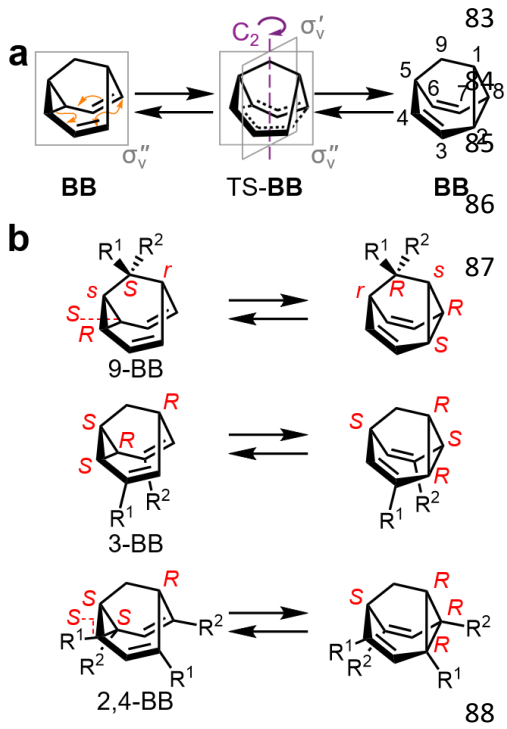

Figure 1 | Multiple Dynamic sp^3-Carbon Centres. Fluxional sp^3-carbon stereochemistry arises in barbaralanes when (a) the structures interchanged by their Cope rearrangements are (b) desymmetrized with either of the three substitution patterns shown. Cahn–Ingold–Prelog priorities are chosen to be R^1>C>R^2 for the assignment of absolute configuration. 3-BB and 2,4-BB each have four chirotopic (*R*/*S*) centres whereas the 9-BB pattern gives rise to five stereogenic centres of which three are chirotopic and two are achirotopic (*r*/*s*).

Diastereomeric Adaptation

We targeted 9-barbaralol **1** (Fig. 2) as a convenient example of the 9-BB substitution pattern that bears a hydroxyl group for synthetic elaboration. It was synthesized (Scheme S1) by a three-step route from ethynyl magnesium bromide and tropylium tetrafluoroborate, using a gold-catalysed enyne cycloisomerization[36,37] to form the barbaralane backbone. When labelling **1** and subsequent compounds, a single stereochemical descriptor is included to indicate the configuration at position 9 of the barbaralane (Fig. 2a), e.g., (*R*)-**1** and (*S*)-**1**, omitting the additional stereochemical labels of positions 1, 2, 5, and 8 for simplicity (Fig. 1). Treatment of **1** with Mosher's acid chloride (Fig. 2a) produces a set of Mosher's esters **2** in which the configurationally fixed stereocentre is introduced at

a distance of three covalent bonds from the dynamic barbaralane unit. An additional descriptor for the configuration of the Mosher's ester group is included in the labels for **2**. Derivatization with (*S*)-Mosher's acid gives a dynamic mixture of two diastereomers, (*R*,*S*)-**2** and (*S*,*S*)-**2**, while (*R*)-Mosher's acid gives (Fig. 2a) the antipodal mixture, (*S*,*R*)-**2** and (*R*,*R*)-**2**. Solutions of the two antipodal dynamic mixtures give opposite circular dichroism spectra (Fig. 3a), as would be expected.

DFT modelling using the ωB97X-D functional, 6-311++G(d,p) basis set and a CS_2 polarizable continuum solvent model was employed to compare (Table S3) the stereoisomerization energetics of **BB**, **1** and **2**. Using these parameters, the automerization of **BB** is predicted to proceed with an activation energy, $\Delta E^{\ddagger}$, of 41.8 kJ·mol^{-1}, which is ~10 kJ·mol^{-1} higher than the experimentally measured[32] $\Delta G^{\ddagger}$ of 32.3 kJ·mol^{-1}, in keeping with previous DFT investigations.[33,34] DFT methods systematically overestimate the energy barrier to Cope rearrangement of barbaralanes, but nevertheless allow useful comparisons of trends in activation energies and are known to predict accurately the relative ground-state energies of isomers.[33,34] The computationally predicted $\Delta E^{\ddagger}$ values for **1** (41.8 kJ·mol^{-1}) and **2** (42.9 kJ·mol^{-1}) are very similar to **BB**, indicating that the hydroxyl or ester group substitutions at position 9 do not significantly change the rapid kinetics.

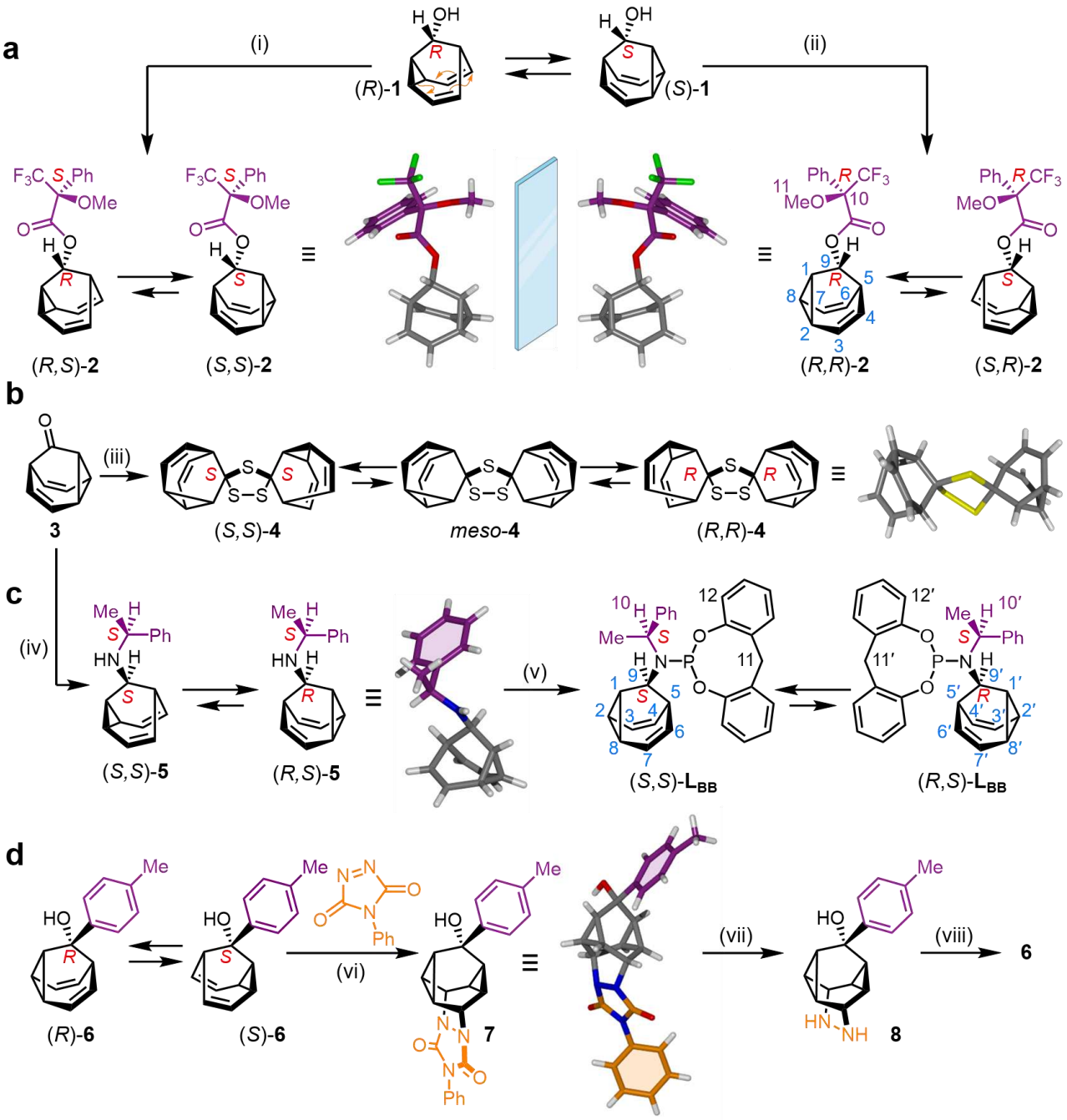

Figure 2 | Diastereomeric Adaptation and Manipulation of Chiral Barbaralanes. (a) Adaptation to a chiral auxiliary, (b) dimerization through a spirocyclic bridge, (c) changing the stereochemical equilibrium by modifying the chiral auxiliary, and (d) reversibly freezing by cycloaddition. Reagents and conditions: (i) 1. (*S*)-MTPA, $(COCl)_2$, hexanes, DMF, rt to −20 °C, 16 h. 2. **1**, DMAP, Et_3N, $CHCl_3$, rt, 5 d, 58%. (ii) 1. (*R*)-MTPA, $(COCl)_2$, hexanes, DMF, rt to −20 °C, 16 h. 2. **1**, DMAP, Et_3N, $CHCl_3$, rt, 3 d, 79%. (iii) **3**, Lawesson's reagent, PhMe, 110 °C, 18 h, 13%. (iv) 1. **3**, (*S*)-1-phenylethylamine, AcOH, MeOH, rt, 30 min. 2. $NaBH_3CN$, 100 °C, 16 h, 89%. (v) **5**, PCl_3, Et_3N, CH_2Cl_2, 0 °C, 3 h. 2. 2,2′-methylenediphenol, CH_2Cl_2, 0 °C to rt, 16 h, 44%. (vi) **6**, PTAD, CH_2Cl_2, 50 °C, 24 h, 85%. (vii) NaOH, ^{i}PrOH, 85 °C, 24 h, taken on crude. (viii) $CuCl_2$, $HCl_{(aq)}$, 0 °C, 4 h, 48% from **7**. X-ray structures are shown in stick representation. Compound **4** crystallizes in a centrosymmetric space group, i.e., (*S*,*S*)-**4** and (*R*,*R*)-**4** are both present, but only (*R*,*R*)-**4** is shown for clarity. Diffraction data for crystals of (*S*,*R*)-**5** allow only assignment of relative stereochemistry. MTPA = α-methoxy-α-trifluoromethylphenylacetic acid. DMF = *N*,*N*-dimethylformamide. DMAP = 4-(dimethylamino)pyridine. PTAD = phenyl-1,2,4-triazoline-3,5-dione.

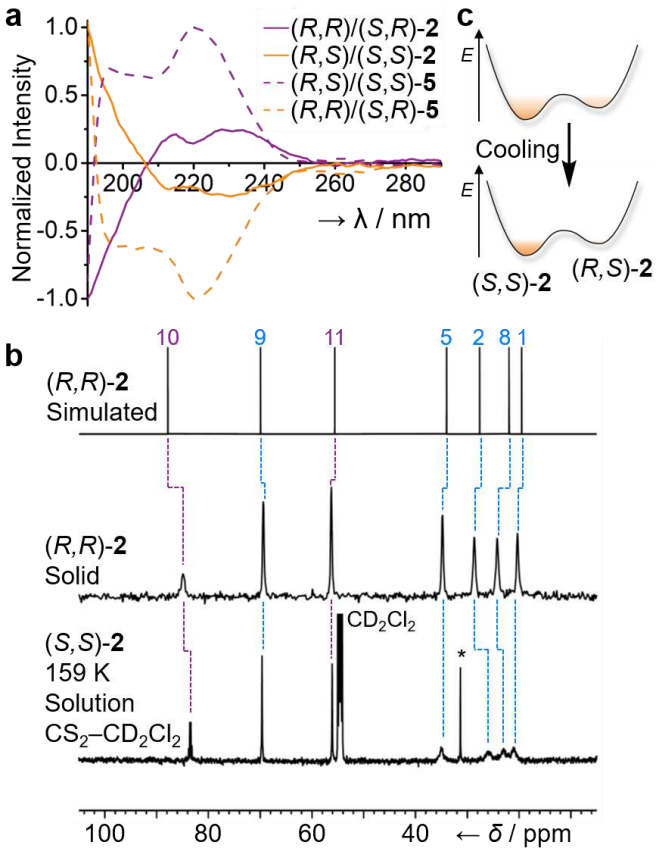

Figure 3 | Spectroscopic Evidence of sp^3-Carbon Adaptation to Covalently Tethered Chiral Auxiliaries. (a) Normalized CD spectra of **2** (115 μM in MeCN) and **5** (210 μM in MeCN) confirm that antipodal equilibrium mixtures give equal and opposite absorbances. (b) Comparison of partial $^{13}C\{^1H\}$ NMR spectra; top, solid-state chemical shifts calculated from the X-ray crystal structure of (*R*,*R*)-**2** in CASTEP v17.2 using the PBE functional and on-the-fly generated pseudopotentials; middle, (*R*,*R*)-**2** as a powder at ambient temperature (105 MHz); bottom, (*S*,*S*)-**2** as a solution in 5:1 CS_2–CD_2Cl_2 at low temperature (125 MHz, 159 K). Resonances are labelled according to the numbering in Fig. 2. *Resonance of residual acetone. (c) The Boltzmann distribution of isomers shifts towards a single stereoisomer at low temperature, e.g., a Gibbs energy difference of ~5 kJ·mol^{-1} would give an approximately 90:10 equilibrium mixture at room temperature, but >98:2 at 159 K, so NMR data would be expected to show a single, major species, as is apparent when comparing the three spectra in (b).

The absence of the σ_v'' mirror plane in **1** is evident (Fig. S45) in its solution-state ^1H NMR spectrum – H_3 and H_7 are magnetically inequivalent, for example. However, the rapid enantiomerization induces a σ_v' mirror plane to the time-averaged structure of **1**, so only six distinct methine resonances are observed. The fixed stereocentre of **2** breaks this σ_v' symmetry. Consequently, nine signals corresponding to the barbaralane methine groups are observed (Fig. S45).

An energy difference, ΔE, of 6.8 kJ·mol^{-1} is computed (Table S3) for the rearrangement of **2**. The influence of the (*S*)-Mosher's ester group moulds the configuration of the cage unit, which preferentially adopts its *S* form, biasing the equilibrium towards (*S*,*S*)-**2**. Consistent with this prediction, a single crystal (Fig. 2a) obtained from the dynamic (*S*)-Moshers's ester mixture was found to contain (*S*,*S*)-**2** as a frozen,[31] single stereoisomer. The equal and opposite outcome is observed from the (*R*)-Mosher's ester mixture, giving the enantiomeric (*R*,*R*)-**2** solid-state structure.

To investigate the nature of the dynamic solution-state mixtures, we compared (Fig. 3b) the solid-

state $^{13}C\{^{1}H\}$ NMR spectrum of enantiopure (*R*,*R*)-**2** crystals to a spectrum obtained using a sample of the (*S*,*S*)-**2** crystals dissolved in 5:1 CS_2–CD_2Cl_2, generating a dynamic mixture of (*R*,*S*)-**2** and (*S*,*S*)-**2**. Cooling the solution to 159 K causes the barbaralane $^{13}C\{^{1}H\}$ NMR resonances to enter the slow exchange regime. As 159 K is only ~20 K below the observed coalescence temperature (Fig. S47) for this low-barrier process, some resonances exhibit exchange broadening. At this low temperature, the decrease of available thermal energy causes the Boltzmann distribution to shift (Fig. 3c) further towards the lowest energy isomer.[31] The solid-state chemical shifts of the barbaralane sp^3-carbons 1, 2, 5, 8, and 9 are assigned (Fig. 3b) by comparison to calculated chemical shifts of (*R*,*R*)-**2**. The resonances of the solution sample match up well with those of (*R*,*R*)-**2** in the solid state, allowing us to assign the resolved solution-state diastereomer as (*S*,*S*)-**2**. The solution-state analysis, therefore, is consistent with the diastereomeric preference predicted by DFT and observed in the solid state.

The dynamic stereochemical equilibrium can also be biased in the absence of a fixed stereogenic element. Dimerization of two 9-BB-type cages through a spirocylic linkage breaks the degeneracy of the equilibrium. By treating (Fig. 2b) barbaralone **3** with Lawesson's reagent, we isolated trithiolane **4**, which undergoes dynamic rearrangements between an achiral isomer, *meso*-**4**, and a pair of enantiomers, (*S*,*S*)-**4** and (*R*,*R*)-**4**. A small ΔE of 0.7 $kJ \cdot mol^{-1}$ is predicted (Table S3) to favour the pair of enantiomers over the *meso* form. Single crystals grown from a solution of **4** contain a racemic mixture of the two chiral stereoisomers.

Further chemical modification to the substituent at position 9 can substantially influence, and even invert, the cage's equilibrium distribution. The phosphoramidite–olefin[38,39] ligand $\mathbf{L_{BB}}$ was synthesized (Fig. 2c) by first subjecting **3** to reductive amination with (*S*)-1-phenylethylamine to afford a mixture of (*S*,*S*)-**5** and (*R*,*S*)-**5**. Sequential treatment of the amine with PCl_3 then 2,2′-methylenediphenol affords $\mathbf{L_{BB}}$. Comparing $\mathbf{L_{BB}}$ to **5** reveals that the differing size and shape of the substituent at position 9 drives the dynamic stereochemical equilibria of the fluxional cage towards opposite configurations. The solution phase equilibrium of the secondary amine is weighted

(Table S3) towards the (*R*,*S*)-**5** diastereomer by a ΔE of 3.1 kJ·mol^{-1}, matching the structure observed by X-ray analysis (Fig. 2c) of a single crystal. By contrast, the (*S*,*S*)-**L$_{BB}$** diastereomer of the phosphoramidite is favoured (Fig. S70) with a ΔE of 14.4 kJ·mol^{-1}. The large magnitude of ΔE for **L$_{BB}$** highlights that the configurational dynamics of the 9-BB motif (Fig. 1) correlate with significant changes in its three-dimensional shape[31] and, therefore, its energy. At the same time, the opposing cage stereochemistry for **5** and **L$_{BB}$** demonstrates that the malleable sp^3-carbon configuration adapts to changes in the nearby steric environment.

Manipulation of Enantiomerization Rates and Transfer of Stereochemistry

To exert further control over the fluxional enantiomerization, we sought to exploit the reactivity of the barbaralanes' skipped diene units. The fluxional rearrangements can be stopped entirely by engaging the alkene units in covalent bonding, whereas coordination of the π-electrons to a transition metal ion[35] modulates the rearrangement rate instead.

An enantiomerizing mixture of 9-(*p*-tolyl)barbaralol **6** engages (Fig. 2d) in a cycloaddition reaction with phenyl-1,2,4-triazoline-3,5-dione,[40] giving rise to **7**. This reaction halts the rearrangement whilst also symmetrizing the structure by forming a second cyclopropyl group. Subsequently, the fluxional cage can be regenerated (Fig. 2c) in a two-step transformation through diazinane **8** (Fig. S44), which undergoes cycloreversion with loss of N_2 upon oxidation with $CuCl_2$. Alternatively, coordination of Pd(II) (Fig. 4) or Ru(II) (Fig. 5) to **L$_{BB}$** causes a reduction in the rate of the Cope rearrangement, as discussed below.

L$_{BB}$ and $PdCl_2$ form (Fig. 4a) a chiral-at-metal[41,42] complex, **L$_{BB}$**$PdCl_2$, linking the sp^3-carbon configurational inversion to the *A*/*C* isomerism[43] of the distorted trigonal bipyramidal (*TBPY*-5-12) coordination environment (Fig. S1). Both possible stereoisomers, arising from coordination of (*S*,*S*)-**L$_{BB}$** or (*R*,*S*)-**L$_{BB}$** through their P centre and an alkene, are observed (Fig. 4a) in the X-ray crystal structure of the $PdCl_2$ complex. The alkene coordination is also evident (Fig. 4b) in the solution state by ^{1}H NMR spectroscopy. For comparison, a monodentate **L$_{BB}$**AuCl complex (Fig. 4a)

was prepared, which shows only small changes in the ^{1}H NMR chemical shifts of its alkene signals H_3 and H_7 relative to the free ligand (Fig. 4c). The room-temperature spectrum of **L$_{BB}$**PdCl$_2$, on the other hand, reveals a large change in the chemical shift of H_7, consistent with coordination of Pd(II) to the alkene on the same face as the phosphoramidite group.

At 240 K, the ^{1}H NMR spectrum reveals (Fig. 4c) the two **L$_{BB}$**PdCl$_2$ isomers in slow exchange. Two sets of signals are observed in a 3:4 ratio, corresponding to a small Gibbs free energy difference, ΔG, of 0.5 kJ·mol^{-1} between the two isomers. Consistent with this observation, DFT calculations predict (Table S3) a small ΔE of 0.9 kJ·mol^{-1} in favour of (*C*,*R*,*S*)-**L$_{BB}$**PdCl$_2$.

Further NMR and DFT analyses elucidate the mechanism by which the **L$_{BB}$**PdCl$_2$ complex isomerizes. Pd(II) salts are known to accelerate Cope rearrangements,[44] doing so by coordinating both alkene groups simultaneously. Coordination of the Pd(II) to one face of the fluxional cage in **L$_{BB}$**PdCl$_2$ evidently has the opposite effect, slowing the Cope rearrangement. Unlike **2**, for example, whose ^{1}H NMR resonances (499 MHz) enter the slow exchange regime below 160 K (Fig. S46), the slower rearrangement of **L$_{BB}$**PdCl$_2$ is resolved by ^{1}H NMR spectroscopy at the higher temperature of 240 K. Using two-dimensional ^{1}H-^{1}H exchange spectroscopy (EXSY) at 240 K (Fig. 4c), we have measured a rate of exchange, k, of 6.48 s^{-1}, indicating a $\Delta G^{\ddagger}$ of 54.6 kJ·mol^{-1} for **L$_{BB}$**PdCl$_2$. The DFT calculated transition state structure, TS-Pd, is consistent with a coordination-coupled Cope (cc-Cope) rearrangement (Fig. 4a) in which the Pd(II) remains bound to the cage. The calculated $\Delta E^{\ddagger}$ of 62.1 kJ·mol^{-1} is an increase of 20.3 kJ·mol^{-1} relative to the **BB** benchmark, which compares well to the experimentally measured increase in $\Delta G^{\ddagger}$ of 22.3 kJ·mol^{-1} (from 32.3 to 54.6 kJ·mol^{-1}). These data indicate that the metal ion 'walks' along one side of the barbaralane cage as the Cope rearrangement proceeds, moving back and forth in sync with the pericyclic reaction. Consequently, the barbaralane not only transmits the stereochemical information from the fixed sp^3-carbon stereocentre through its dynamic sp^3-carbon framework, biasing the chiral-at-metal configuration, it also imparts a novel mechanism of intramolecular configurational change at a pentavalent stereocentre, which differs from the established pseudorotation and turnstile mechanisms.[45]

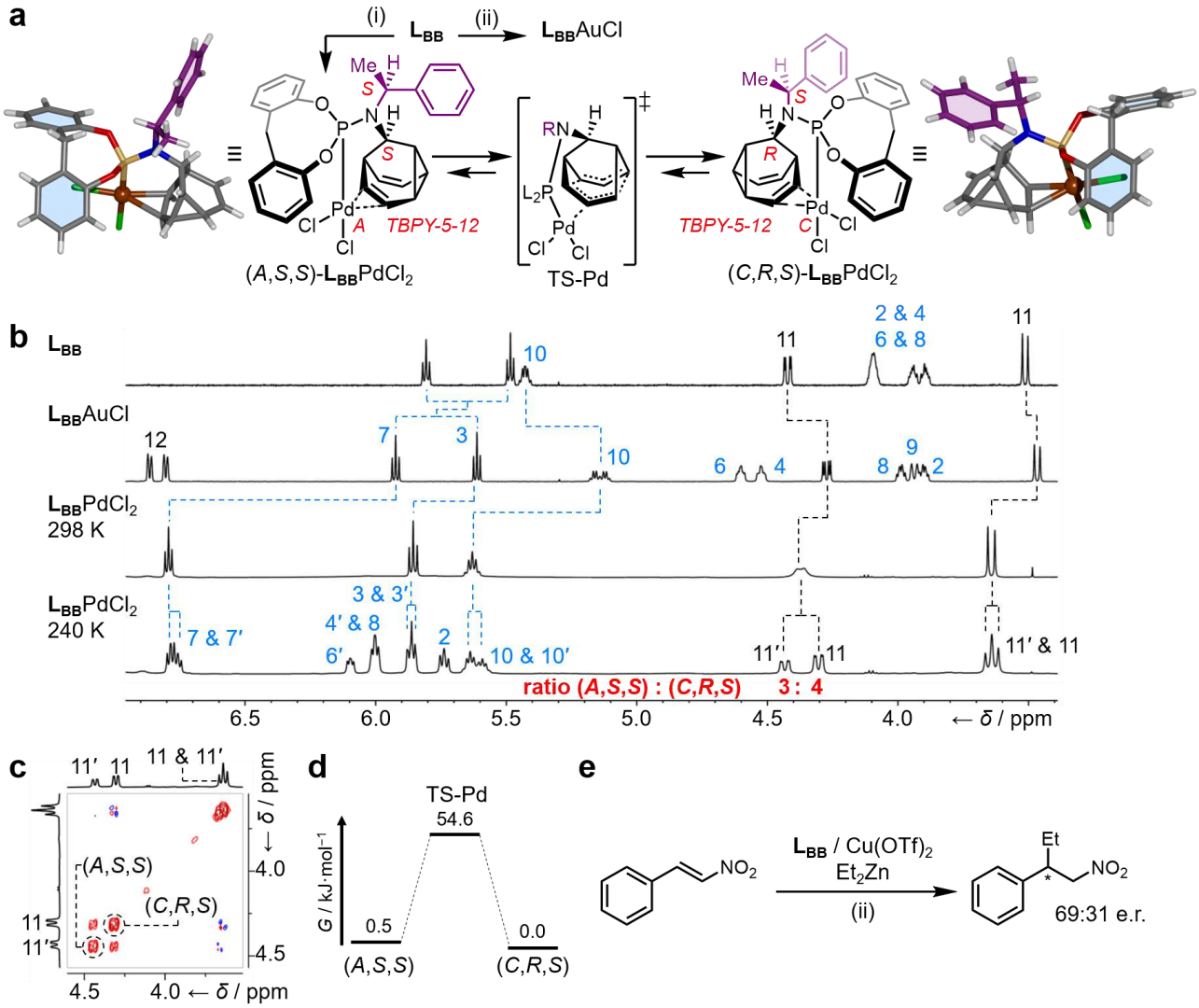

Figure 4 | Transfer of Dynamic sp^3-Carbon Stereochemistry in Au(I), Pd(II), and Cu(II) Complexes. (a) Reagents and conditions: (i) **L**$_{BB}$, $PdCl_2(NCMe)_2$, $CDCl_3$, rt, 15 min, 98%. (ii) **L**$_{BB}$, $Me_2S{\cdot}AuCl$, $CDCl_3$, rt, 10 min, 93%. X-ray crystal structures are shown in stick representation with a ball for metal ions. Solvent molecules are omitted for clarity. Two structurally similar conformers of each **L**$_{BB}PdCl_2$ stereoisomer are present in the unit cell, but only one of each is shown for clarity. (b) Partial ^{1}H NMR ($CDCl_3$) spectra of (top) **L**$_{BB}$ (599 MHz, 298 K), (second) **L**$_{BB}$AuCl (599 MHz, 298 K), (third) **L**$_{BB}PdCl_2$ (499 MHz, 298 K), (bottom) **L**$_{BB}PdCl_2$ (499 MHz, 240 K). Resonances are labelled according to the numbering for **L**$_{BB}$ in Fig. 2. The spectrum at 240 K shows the two **L**$_{BB}PdCl_2$ complexes in slow exchange in a ratio of 3:4. (c) A partial ^{1}H-^{1}H EXSY NMR spectrum (499 MHz, $CDCl_3$, 240 K, mixing time τ_m = 200 ms) showing exchange peaks (red) between resonances of the minor ($H_{11'}$) and major (H_{11}) diastereomers as well as COSY peaks (blue) of geminal proton pairs. (d) Gibbs energy diagram for the cc-Cope rearrangement. (e) Reagents and conditions: (ii) 1. **L**$_{BB}$ (2 mol%), $Cu(OTf)_2$ (2 mol%), PhMe, rt, 30 min. 2. *trans*-β-nitrostyrene, Et_2Zn, hexanes, −78 °C, 12 h, 64%, 69:31 e.r.

Having observed the effective transmission of stereochemical information in **L**$_{BB}$PdCl$_2$, we tested the influence of **L**$_{BB}$ as a ligand for enantioselective catalysis. Phosphoramidite complexes used in enantioselective catalysis routinely comprise two coordinated ligands that each bear two fixed sp^3-carbon stereogenic centres and an atropisomeric biaryl.[38] Remarkably, an equimolar mixture of 2 mol% **L**$_{BB}$ and 2 mol% Cu(OTf)$_2$ catalyse (Fig. 4e) the addition of Et$_2$Zn to *trans*-β-nitrostyrene with an e.r. 69:31. The stereochemical information from the single, fixed stereocentre of the single coordinated ligand is passed through the adaptive **L**$_{BB}$ backbone to the Cu(II) with good fidelity, imparting enantioselectivity to the transformation of the substrates.

The dynamic sp^3-carbon stereochemistry of **L**$_{BB}$ can also be linked to an intermolecular ligand exchange process. Cyclopentadienyl (Cp) half-sandwich Ru(II) complex,[46] **L**$_{BB}$RuCp(NCMe)·PF$_6$ (Fig. 5) has a stereogenic, distorted square pyramidal Ru(II) centre (Fig. S69) coordinated to a labile MeCN ligand. While cc-Cope rearrangements interconvert the *SPY*-5-24 and *SPY*-5-25 configurational isomers[43] (Fig. 5a), MeCN dissociation forms the distorted tetrahedral (*T*-4) chiral-at-metal species **L**$_{BB}$RuCp·PF$_6$, which mediates *A*/*C* stereochemical inversion.

Ru(II) coordination slows the Cope rearrangement sufficiently for a single stereoisomer to be resolved as a metastable species under ambient conditions (Fig. 5b). Upon dissolving single crystals of **L**$_{BB}$RuCp(NCMe)·PF$_6$ obtained by slow evaporation, the ^{1}H NMR spectrum shows the presence of a single complex (Fig. 5b) with resonances distinct from non-coordinated **L**$_{BB}$. After allowing the sample to fully equilibrate at room temperature for four hours, a new set of peaks is observed (Fig. 5b) at a ratio of 4:1 in favour of the initially observed isomer, equivalent to a ΔG of 4.0 kJ·mol^{-1}. X-ray analysis (Fig. 5c) of the crystalline sample reveals the identity of the energetically favoured isomer to be (*C*,*R*,*S*)-**L**$_{BB}$RuCp(NCMe)·PF$_6$. DFT also supports this assignment (Table S3), predicting a ΔE of 6.7 kJ·mol^{-1}.

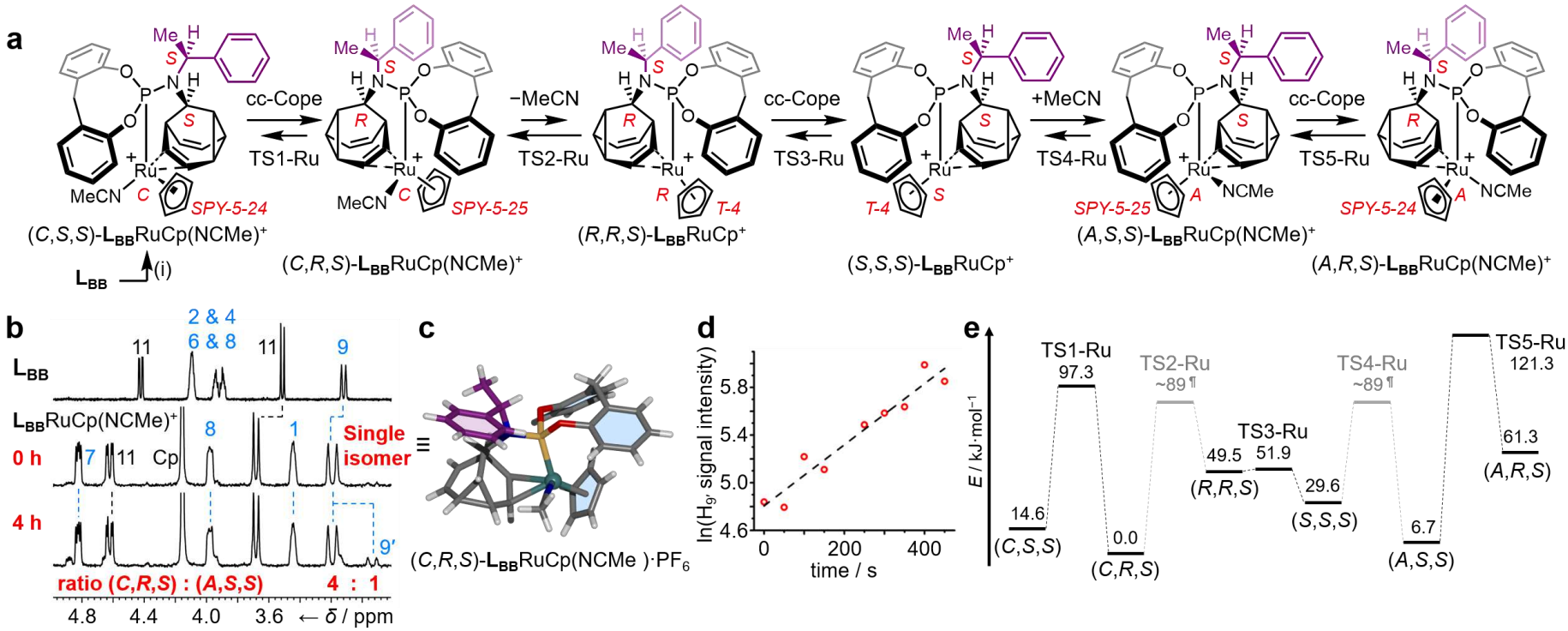

Figure 5 | Transfer of Dynamic sp³-Carbon Stereochemistry in Chiral-at-Ru(II) Complexes. (a) Four diastereomeric square pyramidal complexes are linked by cc-Cope rearrangements and exchange of an MeCN ligand, which proceeds through two intermediate tetrahedral complexes. A non-coordinated PF_6^- counterion is omitted from the structural formula of each complex for clarity. Reagents and conditions: (i) **L**$_{BB}$, $CpRu(NCMe)_3 \cdot PF_6$, $CDCl_3$, rt, 5 min, 69%. (b) Comparison of the partial ^1H NMR ($CDCl_3$) spectra of (top) **L**$_{BB}$ (599 MHz, 298 K), (middle) a sample of **L**$_{BB}$RuCp(NCMe)·PF_6 analysed immediately after dissolving a crystalline sample (400 MHz, 298 K), and (bottom) the same sample after allowing to equilibrate for 4 h (400 MHz, 298 K), revealing that an initially observed single isomer reaches a 4:1 equilibrium mixture. Resonances are labelled according to the numbering for **L**$_{BB}$ in Fig. 2. (c) (*C*,*R*,*S*)-**L**$_{BB}$RuCp(NCMe)·PF_6 is identified in the solid-state X-ray crystal structure, which is shown in stick representation with a ball for the Ru(II) ion. Solvent molecules and the PF_6^- counterion are omitted for clarity. (d) Integration of the ^1H NMR ($CDCl_3$, 400 MHz, 298 K) resonance corresponding to $H_{9'}$ of (*A*,*S*,*S*)-**L**$_{BB}$RuCp(NCMe)·PF_6 upon dissolving a crystalline sample of (*C*,*R*,*S*)-**L**$_{BB}$RuCp(NCMe)·PF_6 reveals a first-order increase in concentration with $k_{obs} = 2.56 \times 10^{-3}$ s^{-1}. (e) A potential energy surface for isomerization based on calculated ΔE and $\Delta E^{\ddagger}$ for the cc-Cope processes (ωB97X-D/6-311++G(d,p)/SDD/CS_2). ¶Experimentally measured (panel d) ligand exchange $\Delta G^{\ddagger}$ values (kJ·mol^{-1}), through TS2-Ru and/or TS4-Ru, are shown for reference.

We measured the isomerization rate of (*C*,*R*,*S*)-**L$_{BB}$**RuCp(NCMe)·PF_6 by monitoring (Fig. 5d) the first-order growth in intensity of the resonance at 3.1 ppm corresponding to the $H_{9'}$ signal of (*A*,*S*,*S*)-**L$_{BB}$**RuCp(NCMe)·PF_6—the isomer calculated (Fig. 5e) to be the next most stable stereoisomer. The observed rate, k_{obs}, of 2.56×10^{-3} s^{-1} at 298 K allows us to determine a $\Delta G^{\ddagger}$ of 87.8 kJ·mol^{-1}. Comparison of this value to maxima of the computed potential energy surface (Fig. 5e), a CD_3CN exchange experiment (Fig. S52), and literature measurements of MeCN dissociation from Cp half-sandwich Ru(II) complexes[46] suggests that the cc-Cope and MeCN exchange processes occur at similar rates. To achieve the (*C*,*R*,*S*)-to-(*A*,*S*,*S*) isomerization observed by NMR, the complex must undergo both cc-Cope and ligand exchange steps (Fig. 5e). Overall, the energetic bias towards (*C*,*R*,*S*)-**L$_{BB}$**RuCp(NCMe)·PF_6 and observation of its stepwise stereomutation to (*A*,*S*,*S*)-**L$_{BB}$**RuCp(NCMe)·PF_6 illustrate that the fluxional sp^3-carbon cage mediates the transfer of stereochemical information with high fiedlity from the single, fixed benzylamino stereocentre through its rigid, tricyclic structure.

Conclusions

The Cope rearrangements of the chiral 9-BB cages simultaneously invert every stereogenic sp^3-carbon centre of their structures. These configurational rearrangements occur rapidly and reversibly, achieving the uncommon property of dynamic sp^3-carbon stereochemistry—one that has remained surprisingly rare since Le Bel[1] and van't Hoff[2] first identified tetrahedral carbon as a source of molecular chirality in 1874. Both the rate of sp^3-carbon inversion and the equilibrium distribution of isomers are sensitive to changes in the 9-BB structure. On one hand, the dynamics of the rearrangement processes are controlled through manipulation of covalent bonding or metal coordination of the 9-BB olefin groups, providing convenient functional handles. On the other hand, the cage adapts its configuration to minimize steric interactions with nearby fixed stereogenic elements and, in so doing, is able to transmit the stereochemical information across its rigid, tricyclic

backbone. When interfaced with transition metal complexes, the dynamic cage conveys a stereochemical preference to the chiral-at-metal[41,42] centre. Controllable and adaptable sp^3-carbon stereochemistry of this kind can be exploited in enantioselective synthesis[7,9,10,28,38,47,48] and chiral functional materials.[49]

References

1. Le Bel, J. A. Sur les relations qui existent entre les formules atomiques des corps organiques, et le pouvoir rotatoire de leurs dissolutions. *Bull. Soc. Chim. Fr.* **22**, 337–347 (1874).
2. van't Hoff, J. H. Sur les formules de structure dans l'espace. *Arch. Néerl.* **9**, 445–454 (1874).
3. Eliel, E. L. & Wilen, S. H. *Stereochemistry of organic compounds*. (Wiley, 1994).
4. Quasdorf, K. W. & Overman, L. E. Catalytic enantioselective synthesis of quaternary carbon stereocentres. *Nature* **516**, 181–191 (2014).
5. Brois, S. J. Aziridines. XII. Isolation of a stable nitrogen pyramid. *J. Am. Chem. Soc.* **90**, 508–509 (1968).
6. Kizirian, J. C. Chiral tertiary diamines in asymmetric synthesis. *Chem. Rev.* **108**, 140–205 (2008).
7. Sibi, M. P., Zhang, R. & Manyem, S. A new class of modular chiral ligands with fluxional groups. *J. Am. Chem. Soc.* **125**, 9306–9307 (2003).
8. Rowley, J. H., Yau, S. C., Kariuki, B. M., Kennedy, A. R. & Tomkinson, N. C. O. Readily accessible chiral at nitrogen cage structures. *Org. Biomol. Chem.* **11**, 2198–2205 (2013).
9. Adachi, S., Takeda, N. & Sibi, M. P. Evaluation of achiral templates with fluxional brønsted basic substituents in enantioselective conjugate additions. *Org. Lett.* **16**, 6440–6443 (2014).
10. Dean, C. *et al.* Readily accessible sp^3-rich cyclic hydrazine frameworks exploiting nitrogen fluxionality. *Chem. Sci.* **11**, 1636–1642 (2020).
11. Fa, S., Egami, K., Adachi, K., Kato, K. & Ogoshi, T. Sequential chiral induction and

regulator-assisted chiral memory of pillar[5]arenes. *Angew. Chem. Int. Ed.* **59**, 20353–20356 (2020).

12. Liang, H. *et al.* Acid/base-tunable unimolecular chirality switching of a pillar[5]azacrown pseudo[1]catenane. *J. Am. Chem. Soc.* **142**, 19772–19778 (2020).

13. Xiao, C. *et al.* Redox-triggered chirality switching and guest-capture/release with a pillar[6]arene-based molecular universal joint. *Angew. Chem. Int. Ed.* **59**, 8094–8098 (2020).

14. Akine, S., Sairenji, S., Taniguchi, T. & Nabeshima, T. Stepwise helicity inversions by multisequential metal exchange. *J. Am. Chem. Soc.* **135**, 12948–12951 (2013).

15. Chen, X. *et al.* A helicate-based three-state molecular switch. *Angew. Chem. Int. Ed.* **57**, 11817–11820 (2018).

16. Katoono, R., Sakamoto, K. & Suzuki, T. Dual dynamic chirality generated in the assembly of three achiral rods through the three-fold twisting of a macrocycle. *Chem. Commun.* **55**, 5503–5506 (2019).

17. Gordon, M. S. & Schmidt, M. W. Does methane invert through square planar? *J. Am. Chem. Soc.* **115**, 7486–7492 (1993).

18. Rasmussen, D. R. & Radom, L. Planar-tetracoordinate carbon in a neutral saturated hydrocarbon: Theoretical design and characterization. *Angew. Chem. Int. Ed.* **38**, 2876–2878 (1999).

19. Walden, P. Ueber die gegenseitige umwandlung optischer antipoden. *Ber. Dtsch. Chem. Ges.* **29**, 133–138 (1896).

20. Kancharla, P. K., Kato, T. & Crich, D. Probing the influence of protecting groups on the anomeric equilibrium in sialic acid glycosides with the persistent radical effect. *J. Am. Chem. Soc.* **136**, 5472–5480 (2014).

21. Sugiyama, S. *et al.* A novel dynamic kinetic resolution accompanied by intramolecular transesterification: Asymmetric synthesis of a 4-hydroxymethyl-2-oxazolidinone from serinol

derivatives. *Tetrahedron* **59**, 3417–3425 (2003).

22. Wolf, C. *Dynamic stereochemistry of chiral compounds*. (RSC Publishing, 2007).

23. Kim, B. *et al.* Stereodynamic quinone-hydroquinone molecules that enantiomerize at sp^3-carbon via redox-interconversion. *J. Am. Chem. Soc.* **139**, 15239–15244 (2017).

24. Gillick-Healy, M. W. *et al.* Two independent orthogonal stereomutations at a single asymmetric center: A narcissistic couple. *Chem. - A Eur. J.* **23**, 2332–2339 (2017).

25. He, M. & Bode, J. W. Racemization as a stereochemical measure of dynamics and robustness in shape-shifting organic molecules. *Proc. Natl. Acad. Sci. U. S. A.* **108**, 14752–14756 (2011).

26. Yahiaoui, O., Patel, H. D., Chinner, K. S., Pašteka, L. F. & Fallon, T. Stereomutation of substituted bullvalenes. *Org. Lett.* **23**, 1157–1162 (2021).

27. Alvarez-Pérez, M., Goldup, S. M., Leigh, D. A. & Slawin, A. M. Z. A chemically-driven molecular information ratchet. *J. Am. Chem. Soc.* **130**, 1836–1838 (2008).

28. Dommaschk, M., Echavarren, J., Leigh, D. A., Marcos, V. & Singleton, T. A. Dynamic control of chiral space through local symmetry breaking in a rotaxane organocatalyst. *Angew. Chem. Int. Ed.* **58**, 14955–14958 (2019).

29. Bismillah, A. N., Chapin, B. M., Hussein, B. A. & McGonigal, P. R. Shapeshifting molecules: The story so far and the shape of things to come. *Chem. Sci.* **11**, 324–332 (2020).

30. Salem, L. *et al.* Narcissistic reactions. *J. Am. Chem. Soc.* **92**, 4472–4474 (1970).

31. Bismillah, A. N. *et al.* Shape-selective crystallisation of fluxional carbon cages. *Chem. Sci.* **9**, 8631–8636 (2018).

32. Günther, H., Runsink, J., Schmickler, H. & Schmitt, P. Applications of ^{13}C NMR spectroscopy. 26. Activation parameters for the degenerate Cope rearrangement of barbaralane and 3,7-disubstituted barbaralanes. *J. Org. Chem.* **50**, 289–293 (1985).

33. Ma, Y. Y. *et al.* Probing the fluxional bonding nature of rapid Cope rearrangements in bullvalene $C_{10}H_{10}$ and its analogs C_8H_8, C_9H_{10}, and C_8BH_9. *Sci. Rep.* **9**, 17074 (2019).

34. Karton, A. Can density functional theory 'Cope' with highly fluxional shapeshifting molecules? *Chem. Phys.* **540**, 111013 (2021).

35. Aumann, R. & Runge, M. Organische synthesen mit übergangsmetall-komplexen, 57. 4,5-Homotropilidene durch intramolekulare cyclopropanierung von (cycloheptatrienylmethyl)carbenchrom-oder-wolfram-komplexen. *Chem. Ber.* **125**, 259–264 (1992).

36. McGonigal, P. R. *et al.* Gold for the generation and control of fluxional barbaralyl cations. *Angew. Chem. Int. Ed.* **51**, 13093–13096 (2012).

37. Ferrer, S. & Echavarren, A. M. Synthesis of barbaralones and bullvalenes made easy by gold catalysis. *Angew. Chem. Int. Ed.* **55**, 11178–11182 (2016).

38. Wakabayashi, K., Aikawa, K., Kawauchi, S. & Mikami, K. Catalyst self-adaptation in conjugate addition to nitroalkenes and nitroacrylates: Instant chirality control in diphenylmethane-based phosphoramidite ligands. *J. Am. Chem. Soc.* **130**, 5012–5013 (2008).

39. Ogasawara, M. *et al.* Phosphine-olefin ligands based on a planar-chiral (π-arene)chromium scaffold: Design, synthesis, and application in asymmetric catalysis. *J. Am. Chem. Soc.* **136**, 9377–9384 (2014).

40. De Bruycker, K. *et al.* Triazolinediones as highly enabling synthetic tools. *Chem. Rev.* **116**, 3919–3974 (2016).

41. Bauer, E. B. Chiral-at-metal complexes and their catalytic applications in organic synthesis. *Chem. Soc. Rev.* **41**, 3153–3167 (2012).

42. Zhou, Z. *et al.* Non-C_2-symmetric chiral-at-ruthenium catalyst for highly efficient enantioselective intramolecular C(sp^3)-H amidation. *J. Am. Chem. Soc.* **141**, 19048–19057 (2019).

43. *Nomenclature of inorganic chemistry: IUPAC recommendations 2005*. (RSC Publishing, 2005).

44. Tantillo, D. J. Speeding up sigmatropic shifts—to halve or to hold. *Acc. Chem. Res.* **49**, 741–749 (2016).

45. Couzijn, E. P. A., Slootweg, J. C., Ehlers, A. W. & Lammertsma, K. Stereomutation of pentavalent compounds: Validating the Berry pseudorotation, redressing Ugi's turnstile rotation, and revealing the two- and three-arm turnstiles. *J. Am. Chem. Soc.* **132**, 18127–18140 (2010).

46. Luginbühl, W. *et al.* Structure and reactivity of ruthenium half-sandwich compounds: Crystal and molecular structure and acetonitrile exchange kinetics and mechanism of Ru(η^6-C_6H_6)$(CH_3CN)_3^{2+}$ and Ru(η^5-C_5H_5)$(CH_3CN)^{3+}$. *Inorg. Chem.* **30**, 2350–2355 (1991).

47. Wang, J. & Feringa, B. L. Dynamic control of chiral space. *Science* **331**, 1429–1432 (2011).

48. Heard, A. W. & Goldup, S. M. Synthesis of a mechanically planar chiral rotaxane ligand for enantioselective catalysis. *Chem* **6**, 994–1006 (2020).

49. Morrow, S. M., Bissette, A. J. & Fletcher, S. P. Transmission of chirality through space and across length scales. *Nat. Nanotechnol.* **12**, 410–419 (2017).

Acknowledgments

A.N.B. and A.T.T. acknowledge Engineering and Physical Sciences Research Council (EPSRC) doctoral training grants. A.N.B. acknowledges grant support from Funds for Women Graduates. B.A.H. and H.C.W. thank the EPSRC Centres for Doctoral Training in Soft Matter and Functional Interfaces (SOFI) and Renewable Energy Northeast Universities (ReNU), respectively, for PhD studentships. B.A.H. acknowledges postgraduate scholarship support from the Society of Chemical Industry (SCI) and the Natural Sciences and Engineering Research Council of Canada (NSERC). A.N.B. and P.R.M. acknowledge the support of a Leverhulme Trust Research Project Grant (RPG-2020-218). We are grateful to Dr David Apperley for assistance with solid-state NMR measurements and Mr Lennox Lauchlan for chiral HPLC.

Author contributions

A.N.B. synthesized **3** and **6**, carried out variable-temperature NMR spectroscopy, and prepared the supplementary information. T.G.J. synthesized **2**, **4**, and **5**, and performed CD spectroscopy. B.A.H. and A.T.T. optimized trapping and release of **6** by cycloaddition. A.N.B., A.T.T. and H.C.W. performed preliminary experiments. J.A.A. assisted with NMR measurements. D.S.Y. solved X-ray crystal structures. P.R.M. conceived and directed the research, synthesized and analysed **L$_{BB}$** and its metal complexes, performed the enantioselective catalysis, carried out DFT calculations, and wrote the manuscript. All authors analysed data and revised the manuscript.

Competing financial interests

The authors declare no competing financial interests.

Author ORCID iDs

Aisha N. Bismillah – 0000-0002-0588-4939

Toby G. Johnson – 0000-0002-6475-769X

Burhan A. Hussein – 0000-0002-4938-7379

Andrew T. Turley – 0000-0001-6492-7727

Ho Chi Wong – 0000-0003-3600-0777

Juan A. Aguilar – 0000-0001-9181-8892

Dmitry S. Yufit – 0000-0002-7208-1212

Paul R. McGonigal – 0000-0002-8538-7579

CCDC Numbers for Crystallographic Data

2068012 – **1**

2068013 – **4**

2068014 – (*S*,*R*)-**5**

2068015 – (*R*,*S*)-**2**

2068016 – (*S*,*R*)-**2**

2068017 – **7**

2068018 – $\mathbf{L_{BB}}PdCl_2$

2068019 – **S2** (see Supplementary Information)

2068020 – (*C*,*R*,*S*)-$\mathbf{L_{BB}}RuCp(NCMe)\cdot PF_6$

Figures

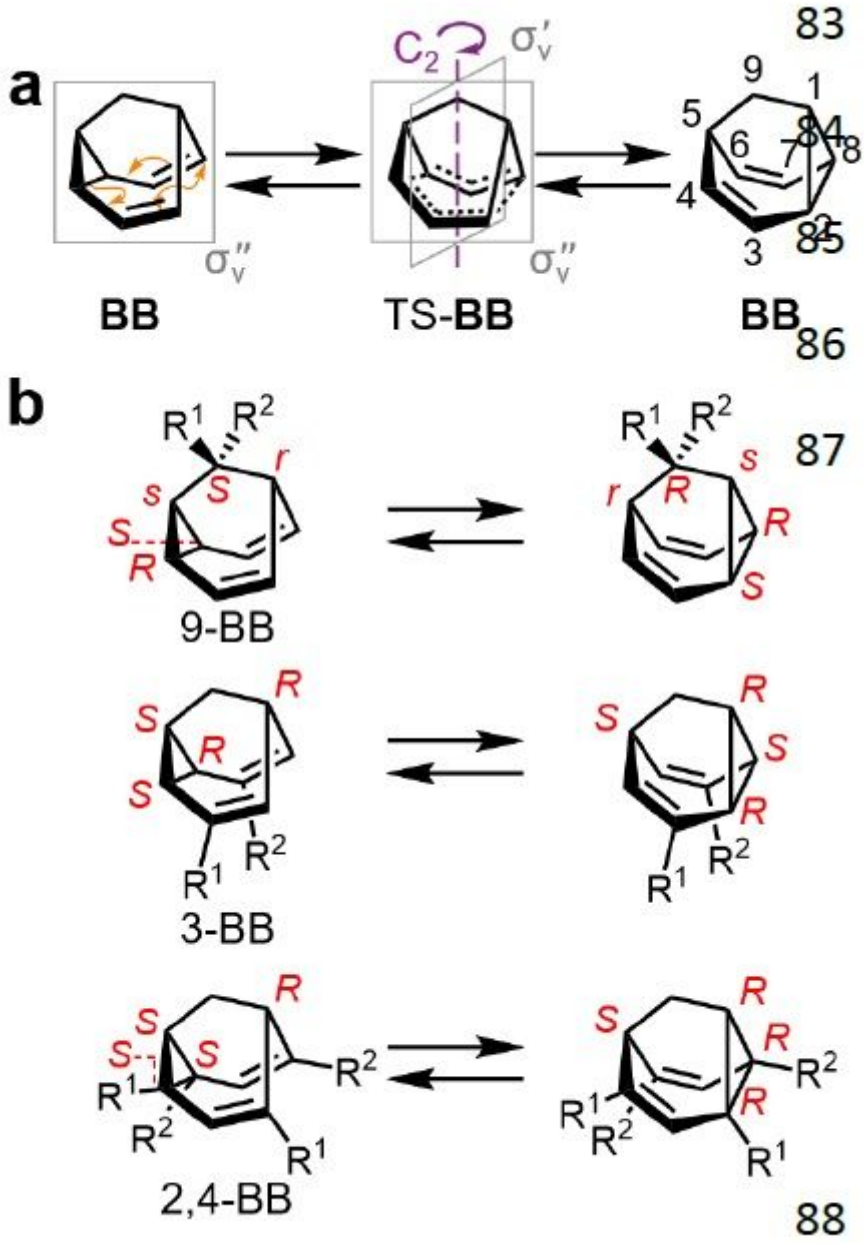

Figure 1

Multiple Dynamic sp3-Carbon Centres. Fluxional sp3-carbon stereochemistry arises in barbaralanes when (a) the structures interchanged by their Cope rearrangements are (b) desymmetrized with either of the three substitution patterns shown. Cahn–Ingold–Prelog priorities are chosen to be R1>C>R2 for the assignment of absolute configuration. 3-BB and 2,4-BB each have four chirotopic (R/S) centres whereas the 9-BB pattern gives rise to five stereogenic centres of which three are chirotopic and two are achirotopic (r/s).

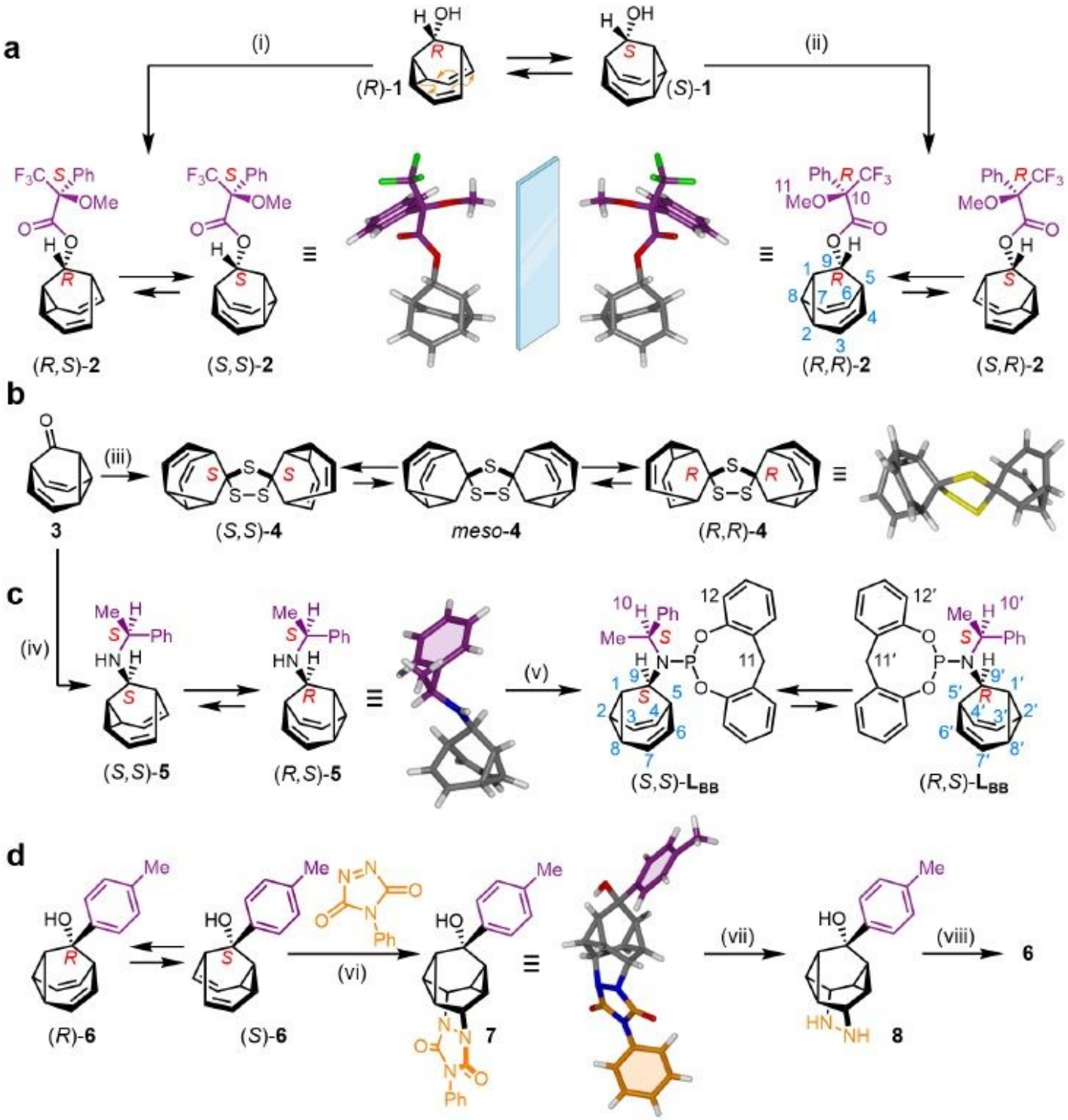

Figure 2

Diastereomeric Adaptation and Manipulation of Chiral Barbaralanes. (a) Adaptation to a chiral auxiliary, (b) dimerization through a spirocyclic bridge, (c) changing the stereochemical equilibrium by modifying the chiralauxiliary, and (d) reversibly freezing by cycloaddition. Reagents and conditions: (i) 1. (S)-MTPA, (COCl)2, hexanes, DMF, rt to −20 °C, 16 h. 2. 1, DMAP, Et3N, CHCl3, rt, 5 d, 58%. (ii) 1. (R)-MTPA, (COCl)2, hexanes, DMF, rt to −20 °C, 16 h. 2. 1, DMAP, Et3N, CHCl3, rt, 3 d, 79%. (iii) 3, Lawesson's reagent, PhMe,

110 °C, 18 h, 13%. (iv) 1. 3, (S)-1-phenylethylamine, AcOH, MeOH, rt, 30 min. 2. NaBH3CN, 100 °C, 16 h, 89%. (v) 5, PCl3, Et3N, CH2Cl2, 0 °C, 119 3 h. 2. 2,2'-methylenediphenol, CH2Cl2, 0 °C to rt, 16 h, 44%. (vi) 6, PTAD, CH2Cl2, 50 °C, 24 h, 85%. (vii) NaOH, iPrOH, 85 °C, 24 h, taken on crude. (viii) CuCl2, HCl(aq), 0 °C, 4 h, 48% from 7. X-ray structures are shown in stick representation. Compound 4 crystallizes in a centrosymmetric space group, i.e., (S,S)-4 and (R,R)-4 are both present, but only (R,R)-4 is shown for clarity. Diffraction data for crystals of (S,R)-5 allow only assignment of relative stereochemistry. MTPA = α-methoxy-α-trifluoromethylphenylacetic acid. DMF = N,N-dimethylformamide. DMAP = 4-(dimethylamino)pyridine. PTAD = phenyl‐1,2,4‐triazoline‐3,5‐dione.

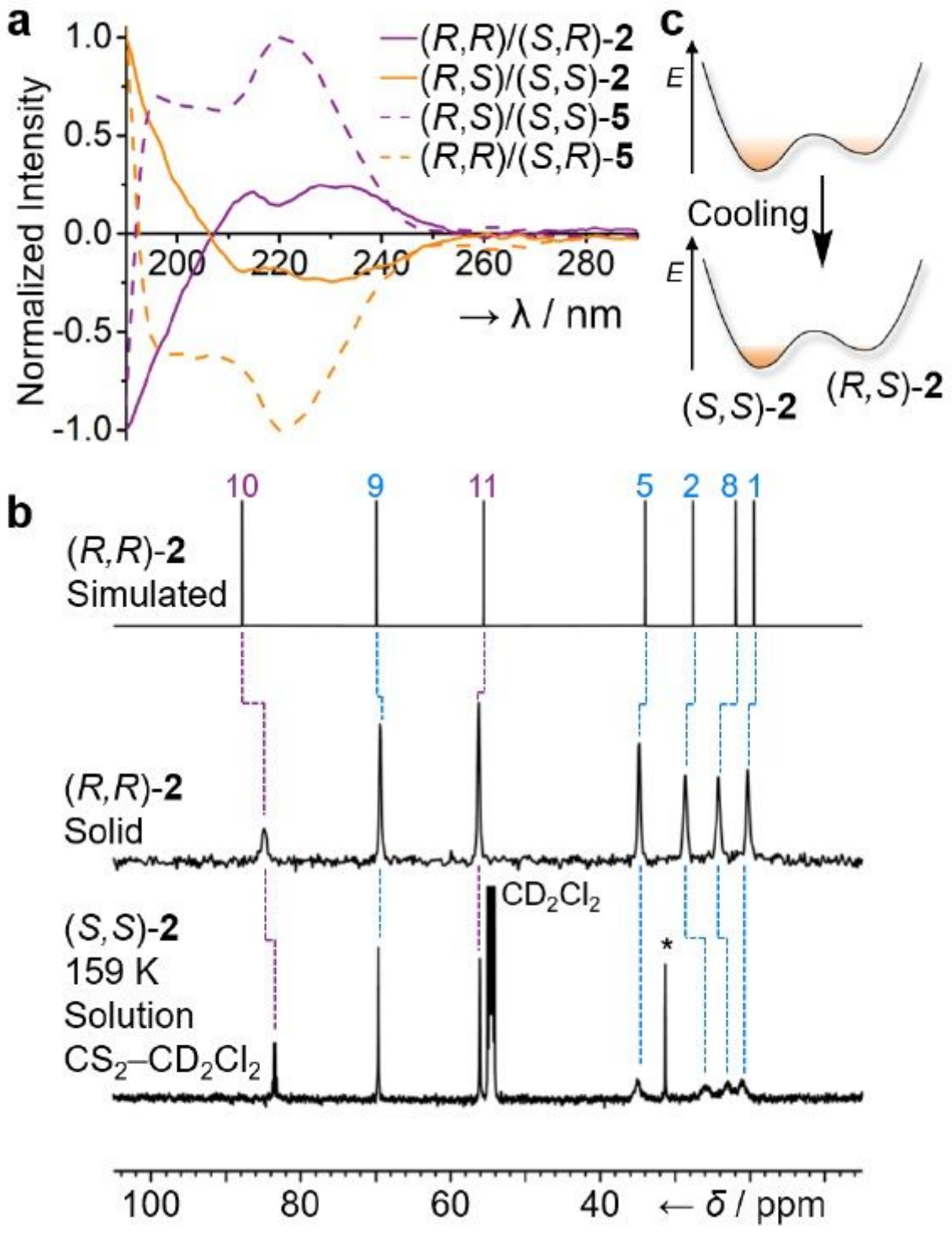

Figure 3

Spectroscopic Evidence of sp3-Carbon Adaptation to Covalently Tethered Chiral Auxiliaries. (a) Normalized CD spectra of 2 (115 μM in MeCN) and 5 (210 μM in MeCN) confirm that antipodal equilibrium mixtures give equal and opposite absorbances. (b) Comparison of partial 13C{1H} NMR spectra; top, solid-state chemical shifts calculated from the X-ray crystal structure of (R,R)-2 in CASTEP v17.2 using the PBE functional and on-the-fly generated pseudopotentials; middle, (R,R)-2 as a powder at

ambient temperature (105 MHz); bottom, (S,S)-2 as a solution in 5:1 CS2–CD2Cl2 at low temperature (125 MHz, 159 K). Resonances are labelled according to the numbering in Fig. 2. *Resonance of residual acetone. (c) The Boltzmann distribution of isomers shifts towards a single stereoisomer at low temperature, e.g., a Gibbs energy difference of ~5 kJ·mol−1 would give an approximately 90:10 equilibrium mixture at room temperature, but >98:2 at 159 K, so NMR data would be expected to show a single, major species, as is apparent when comparing the three spectra in (b).

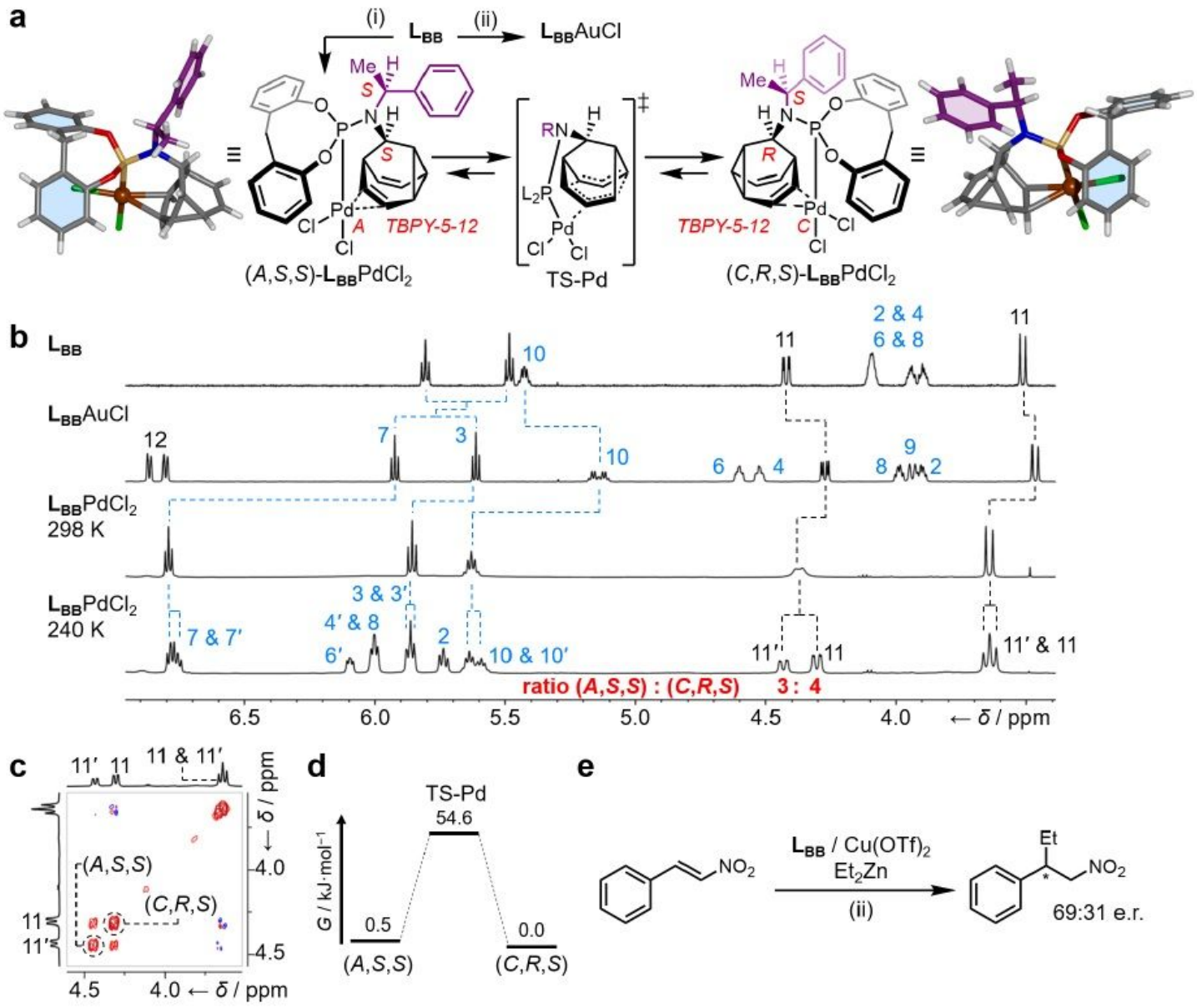

Figure 4

Transfer of Dynamic sp3-Carbon Stereochemistry in Au(I), Pd(II), and Cu(II) Complexes. (a) Reagents and conditions: (i) LBB, PdCl2(NCMe)2, CDCl3, rt, 15 min, 98%. (ii) LBB, Me2S·AuCl, CDCl3, rt, 10 min, 93%. X-ray crystal structures are shown in stick representation with a ball for metal ions. Solvent molecules are omitted for clarity. Two structurally similar conformers of each LBBPdCl2 stereoisomer are present in the unit cell, but only one of each is shown for clarity. (b) Partial 1H NMR (CDCl3) spectra of (top) LBB (599

MHz, 298 K), (second) LBBAuCl (599 MHz, 298 K), (third) LBBPdCl2 (499 MHz, 298 K), (bottom) LBBPdCl2 (499 MHz, 240 K). Resonances are labelled according to the numbering for LBB in Fig. 2. The spectrum at 240 K shows the two LBBPdCl2 complexes in slow exchange in a ratio of 3:4. (c) A partial 1H-1H EXSY NMR spectrum (499 MHz, CDCl3, 240 K, mixing time τm = 200 ms) showing exchange peaks (red) between resonances of the minor (H11') and major (H11) diastereomers as well as COSY peaks (blue) of geminal proton pairs. (d) Gibbs energy diagram for the cc-Cope rearrangement. (e) Reagents and conditions: (ii) 1. LBB (2 mol%), Cu(OTf)2 (2 mol%), PhMe, rt, 30 min. 2. trans-β-nitrostyrene, Et2Zn, hexanes, −78 °C, 12 h, 64%, 69:31 e.r.

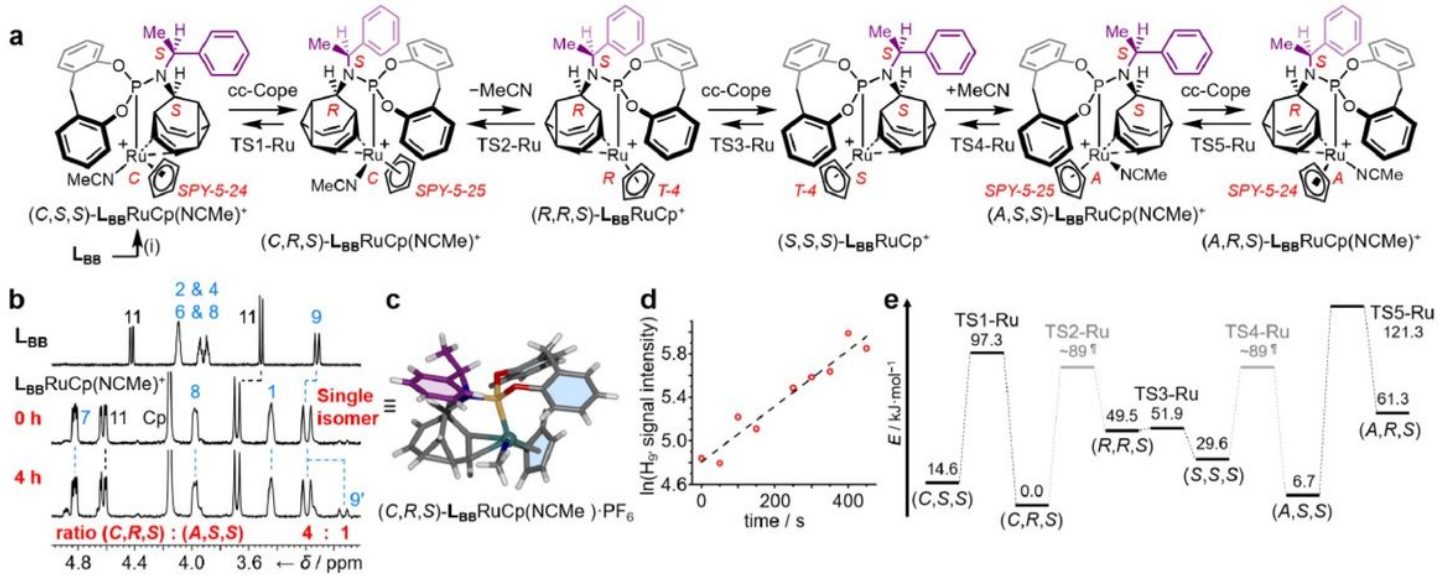

Figure 5

Transfer of Dynamic sp3-Carbon Stereochemistry in Chiral-at-Ru(II) Complexes. (a) Four diastereomeric square pyramidal complexes are linked by cc-Cope rearrangements and exchange of an MeCN ligand, which proceeds through two intermediate tetrahedral complexes. A non-coordinated PF6− counterion is omitted from the structural formula of each complex for clarity. Reagents and conditions: (i) LBB, CpRu(NCMe)3·PF6, CDCl3, rt, 5 min, 69%. (b) Comparison of the partial 1H NMR (CDCl3) spectra of (top) LBB (599 MHz, 298 K), (middle) a sample of LBBRuCp(NCMe)·PF6 analysed immediately after dissolving a crystalline sample (400 MHz, 298 K), and (bottom) the same sample after allowing to equilibrate for 4 h (400 MHz, 298 K), revealing that an initially observed single isomer reaches a 4:1 equilibrium mixture. Resonances are labelled according to the numbering for LBB in Fig. 2. (c) (C,R,S)-LBBRuCp(NCMe)·PF6 is identified in the solid-state X-ray crystal structure, which is shown in stick representation with a ball for the Ru(II) ion. Solvent molecules and the PF6− counterion are omitted for clarity. (d) Integration of the 1H NMR (CDCl3, 400 MHz, 298 K) resonance corresponding to H9' of (A,S,S)-LBBRuCp(NCMe)·PF6 upon dissolving a crystalline sample of (C,R,S)-LBBRuCp(NCMe)·PF6 reveals a first-order increase in concentration with kobs = 2.56 × 10−3 s−1. (e) A potential energy surface for isomerization based on calculated ΔE and ΔE‡ for the cc-Cope processes (ωB97X-D/6- 311++G(d,p)/SDD/CS2). ¶Experimentally

measured (panel d) ligand exchange ΔG‡ values (kJ·mol−1), through TS2-Ru and/or TS4-Ru, are shown for reference.

Supplementary Files

This is a list of supplementary files associated with this preprint. Click to download.

- SIBismillahetalDynamicsp3CStereochemistry.pdf
- SIBismillahetalDynamicsp3CStereochemistry.pdf
- AllStructuresNCHEM21030456.cif
- NCHEM21030456CrystallographicData.zip
- NCHEM21030456SIBismillahetalDynamicsp3CStereochemistry.pdf